Multi-Sampled Grid-Connected VSCs: A Path Toward Inherent Admittance Passivity

Ivan Z. Petric, *Student Member, IEEE*, Paolo Mattavelli, *Fellow, IEEE*, and Simone Buso, *Member, IEEE*

***Abstract*—This article investigates the capability of multi-sampled pulsewidth modulator (MS-PWM) control to improve the input admittance properties of voltage source converters (VSCs). Due to delays found in digital control systems, the VSC admittance features a negative real part above a certain frequency, which may result in lowly damped or even unstable grid dynamics. To prevent the occurrence of harmonic instability, recent standards require the admittance of every grid-connected VSC to behave as a passive network. In this article, it is shown that the MS-PWM control significantly improves passivity measures by reducing the overall system delay. The passive behavior is achieved effortlessly, using a single-stage control loop. This avoids the need for passive or active damping techniques, which are associated with increased losses and number of sensors, sensitivity to noisy measurements, ambiguity of damping filter design, and overall system complexity. The experimental verification, performed on a two-level single-phase VSC, shows a very good match between admittance measurements and analytic modeling even above the switching frequency. Grid-connected operation is tested to demonstrate the improvement of resonance damping obtained with MS-PWM control.**

***Index Terms*—Admittance measurements, multi-sampled pulsewidth modulators (MS-PWM), passivity, stabilization, voltage source converters (VSCs).**

I. INTRODUCTION

EXISTING power systems are experiencing a great change due to the increasing presence of power electronic converters. These devices are more and more necessary to fully exploit renewable energy resources, enable electrification of transportation, and the storage of electrical energy, among other functions [1], [2]. Heavy presence of voltage source converters (VSCs), connected to ac distribution networks, rises some concern as it is known that, due to the interaction between various grid-connected converters, harmonic instability may arise and compromise the system operation [3]. This may occur, for example, when control systems of grid-tied VSCs introduce negative damping at frequencies of poorly damped grid resonances. In the low-frequency range, negative damping is introduced by the phase-locked loop (PLL) of inverters and the constant power control of rectifiers [3], [4]. In the high-frequency range, negative damping is caused by the time delay and current control loop dynamics (in case of grid-following converters) [3], [5]. Digital control systems introduce delays due to analog-to-digital conversion (ADC), algorithm computation time, and modulation delay [6].

For stability analysis of systems with interconnected power converters, the impedance-based approach is found to be very effective [5], [7]–[13]. It consists of representing each converter with its Norton or Thevenin equivalent circuit and assessing the system stability properties by analyzing the resulting admittance network. A sufficient, but not necessary, condition for the system stability is obtained if each admittance is passive, i.e., its real part is nonnegative [for single-input single-output (SISO) systems] [4], [14]–[17]. Based on these considerations, in some countries, the heavy impact of grid-tied VSCs on the traction system stability has resulted in the requirement to comply with input admittance passivity standards [18].

To enable admittance passivity, additional damping must be provided in the frequency range of interest. To achieve this, without resorting to adding losses to the system, many strategies of active damping (AD) have been developed [4], [14]–[17], [19]–[25]. These strategies are focused on compensating digital delays using phase-lead filters. Single-loop AD relies on compensating delays by introducing derivative action to the controller structure [20]. This can help render the admittance passive at medium frequencies; however, due to discrete derivative behavior, it strongly deteriorates passivity at high frequencies, close to the Nyquist frequency. For this reason, to try to expand the passivity region up to the Nyquist frequency, multiloop-based AD is generally implemented [4], [14]–[17], [22], [23]. It relies on using additional feedforward or feedback to compensate the impact of time delays. This often includes derivative action being applied to the voltage at the point of common coupling (PCC), which may bring practical implementation problems, as those caused by large quantization levels and excessive measurement noise. Admittance passivity up to the Nyquist frequency is first claimed in [14]. However, this method requires derivative action to be applied in analog domain or using oversampling. Additionally, derivative gain is applied in cascade with a biquad filter, which further complicates the system structure and parameter design.

Manuscript received September 14, 2021; revised November 26, 2021; accepted January 15, 2022. Date of publication January 25, 2022; date of current version March 24, 2022. This work was supported in part by the Project MultiportGrid "Cross-Sectoral Energy Control through Interconnected Microgrids by Multiport Converter" funded within the call "ERA-Net Smart Energy Systems RegSys Joint Call 2018" and in part by MIUR (Italian Minister for Education) under the initiative "Departments of Excellence" (Law 232/2016). Recommended for publication by Associate Editor B. P. McGrath. *(Corresponding author: Ivan Z. Petric.)*

Ivan Z. Petric and Simone Buso are with the Department of Information Engineering, University of Padova, 35131 Padova, Italy (e-mail: ivan.petric@phd.unipd.it; simone.buso@dei.unipd.it).

Paolo Mattavelli is with the Department of Management and Engineering, University of Padova, 36100 Vicenza, Italy (e-mail: mattavelli@ieee.org).

Color versions of one or more figures in this article are available at https://doi.org/10.1109/TPEL.2022.3145191.

Digital Object Identifier 10.1109/TPEL.2022.3145191

In [15], a similar method is shown, which improves passivity using the PCC voltage feedforward with discretized derivative action, without oversampling. Different parameter designs compared with the work in [14] is given, which requires a fixed current loop bandwidth and is prone to parameter sensitivity due to double pole-zero cancelation. Without adding resistances, the method from the work in [15] brings improvements at medium frequencies, but again deteriorates the admittance properties close to the Nyquist frequency. In [16] and [22], the procedure from the work in [14] is generalized and oversampled/analog derivative is avoided using the capacitor current feedback. This limits its use to applications with *LCL* filters, requires additional sensors, and may impact the closed-loop stability. All AD methods introduce a significant complexity to the control system structure and practical implementation issues. Furthermore, the required design of filters that render the admittance passive is not straightforward and generally applicable.

With the advancement of digital control platforms, increasingly more information can be processed within a switching interval of a VSC. This has led to development of multi-sampled pulsewidth modulator (MS-PWM) control, where the feedback is sampled and the control action is performed more than two times per switching period [26]–[36]. MS-PWM reduces control and modulation delays, enabling analoglike dynamic properties using digital control systems. This article investigates the capability of MS-PWM control to render the admittance passive, by inherently reducing, instead of compensating, digital delays. It is shown that the increase of the oversampling factor improves the passivity, by boosting the admittance phase even above the switching frequency. In this way, passivity is achieved almost effortlessly, without parameter sensitivity, and the design of the current control loop can be performed solely based on the required closed-loop performance. The experimental verification is performed on a single-phase, two-level, grid-following VSC with an inductive filter. The performed admittance measurements show an excellent agreement with the analytic modeling. With MS-PWM, certain nonlinearities may arise due to vertical intersections between the modulating waveform and the carrier [27], [32], [33], [36]. The impact of these nonlinearities on admittance passivity is analyzed and no detrimental impact is found; just some mismatch from analytical modeling is seen, mainly for lower values of oversampling factors.

The rest of this article is organized as follows. Section II presents the multi-sampled control system of a VSC. Section III presents the analytic modeling of a grid-connected VSC, using its Norton equivalent representation. The current controller is designed based on the closed-loop requirements. In the end, the admittance is analyzed using a passivity index and the impact of system parameters on it is explained. Section IV features experimental validation of the presented theory. The VSC admittance is measured for various values of the oversampling factor, in a wide frequency range. The circuit used for admittance measurements, which also allows the investigation of MS-PWM nonlinearities, is described. Grid-connected operation is tested, to demonstrate how the increase of the oversampling factor results in better resonance damping. Finally, Section V concludes this article.

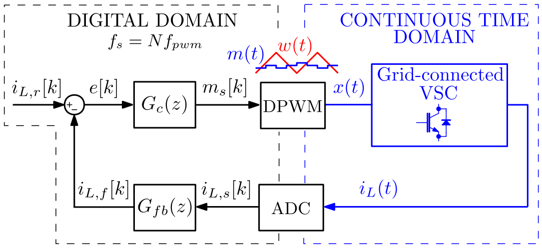

Fig. 1. Block diagram of MS-PWM single-loop current control system of a two-level, single-phase, grid-following VSC.

II. MS-PWM CONTROL

The MS-PWM can be implemented for any converter topology, including multilevel and multiphase systems. The multi-sampled single-loop current control system of a two-level, single-phase, grid-following VSC is shown in Fig. 1. An inductive output filter is assumed. An ADC is used to transform the inductor current i_L from continuous to digital domain. The digital domain operates at sampling frequency $f_s = Nf_{\text{pwm}}$, where N is the multisampling (oversampling) factor, and f_{pwm} is the switching frequency. The control period is defined as $T_s = \frac{1}{f_s}$. The digital domain may comprise a feedback filter $G_{fb}(z)$, reference point $i_{L,r}$, and controller $G_c(z)$.[1] The digital pulsewidth modulator (DPWM) serves as an interface from digital to continuous domain. Its inherent zero-order hold function transforms m_s into m, which is compared with the carrier w to provide the switching signal x. The switching signal, used to drive the transistors, is a square waveform with duty cycle D. It is assumed that w is scaled by its maximum value, and m is limited inside the range $[0, 1]$. To prevent multiple switching from occurring, switching action is always determined based on first intersection between m and w, for each slope of the carrier. This is equivalent to allowing turn-ON only during the negative slope of the carrier, and turn-OFF only during the positive one.

A. Impact of MS-PWM on Delay Reduction

In this article, the triangular carrier is used, due to its favorable properties in MS-PWM applications [27]. The small-signal model of the MS-PWM with the triangular carrier can be obtained using the describing function approach [27], [37]

$$G_{\text{DPWM}}(s) = \frac{d(s)}{m(s)} = A(s, D, N)e^{-s\frac{T_s}{2}} \approx e^{-s\frac{T_{\text{pwm}}}{2N}} \tag{1}$$

where d is the continuous-time duty cycle of $x(t)$, used in averaged modeling [6], and s is the complex variable of the Laplace transform. The gain A depends on N and D, but is closely approximated as unity gain [27]. From (1), it can be seen that with increase of N, MS-PWM approaches the naturally sampled (analog) PWM, which does not bring any phase lag [38]. This modeling approach allows us to obtain intuitive insights on the

---

[1] The controller outputs the reference voltage v_r, which is scaled with the input voltage to obtain the digital modulating waveform m_s. The controller may feature computation delay [6]. The delay and scaling with the input voltage are not shown in the illustration.

DPWM impact on admittance properties. Furthermore, excellent match between analytical values and admittance measurements is obtained in the experimental section. However, if even greater precision is required, models that take into account the multirate structure of the system, sampling, and PWM sidebands can be used in place of (1) [5], [12], [39]–[42].

Often, due to algorithm execution time, update of m is delayed by one control period [6]. This brings an additional delay equal to $T_s = \frac{T_{\text{pwm}}}{N}$. Delays due to modulation and algorithm calculation can be combined, which yields the total time delay of MS-PWM control system

$$\tau_D = \frac{3}{2}\frac{T_{\text{pwm}}}{N}. \tag{2}$$

The fact that the total time delay is inversely proportional to N provides motivation to investigate MS-PWM. The maximum achievable N depends on the available processing power relative to the switching frequency. Some application scenarios are more likely to allow high values of N (e.g., high-power converters) than others (e.g., high-switching-frequency converters).

It should be mentioned that delay reduction can also be obtained by updating m instantly after computation, if powerful control platforms are employed [6], [43]. However, this does not reduce the modulation delay, determined by (1). Additionally, other types of modulators exist, with structures that bring small-signal phase-lead [44]–[46]. The impact of these modulators on the VSC admittance is currently being investigated.

B. Sampling-Induced MS-PWM Nonlinearities

For two-level converters, only two sampling instants per PWM period yield the average value of i_L. Therefore, as N is increased above 2, the switching ripple is unavoidably introduced in the feedback. Effects of ripple in the feedback have been well-investigated for naturally sampled PWM and similar properties are expected for MS-PWM, especially as N is increased to high values [28], [29], [40], [47], [48].

Besides this, MS-PWM brings some unique nonlinear effects, which are particularly evident for lower values of N [36]. Due to asymmetry of the switching impulse with respect to the carrier, average of N samples of $i_{L,s}[k]$ may not correspond to the average of $i_L(t)$ over the observed switching period. This causes aliasing that can have impact on the steady-state error, which may be compensated by outer control loops. In [34], it is shown that aliasing causes current distortion in grid-tied converters, although with a limited impact compared to other nonlinearities, such as dead times [36]. These issues are out of the scope of this article; however, it should be mentioned that the aliasing may also occur in case of double-sampled PWM, due to asymmetry between x and w [6]. Additionally, as N is increased, aliasing issues are decreased as the average value of the sampled feedback comes closer to the true average value.

Other nonlinear effects, in this article referred to as the MS-PWM nonlinearities, are caused by the discontinuity of the sampled modulating waveform and are localized around specific critical values of duty cycles [36]. MS-PWM nonlinearities arise when vertical intersections between m and w occur. An example of this operation can be seen in Fig. 2, where a counter-phase vertical crossing between w and m prevents the modulation of the rising edge of x, reducing the effective modulator small-signal gain [27], [36]. The counter-phase attribute refers to the fact that the slopes of m and w have opposite signs at the intersection instant. A detailed analysis of types of vertical intersections, their impact on transient and steady-state operation, and control loop settings that enable or suppress each of them can be read in [36]. Note that in DSP applications, switching action is often determined using an equality comparison between m and w. This requires additional logic to predict the upcoming vertical crossing and force the change of x at the beginning of the following update instant, thus preventing pulse-skipping [26]. In field-programmable gate array applications, equality is easily replaced with a "greater-than" comparison. As well as for aliasing, impact of MS-PWM nonlinearities is strongly reduced by increasing the value of N, as discontinuities are brought down and modulating waveform starts to closely resemble the one found in naturally sampled PWM.

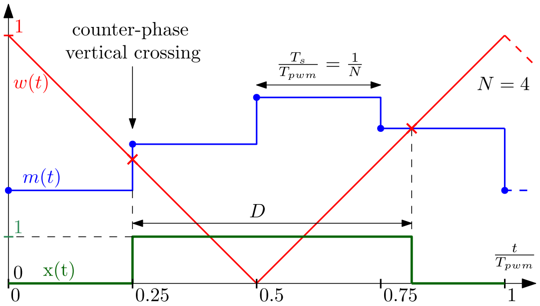

Fig. 2. Illustration of MS-PWM operation for $N = 4$. A counter-phase vertical crossing occurs for the turn-ON edge of x, which reduces the small-signal modulator gain.

Most of the sampling-induced MS-PWM nonlinearities are strongly suppressed by compensating the switching ripple, which, however, counteracts the delay reduction [28], [34]. In [36], it is shown that MS-PWM can operate well even without filtering the switching ripple, which is why the same approach is followed in this article. In this way, the impact of nonlinearities on admittance measurements is directly examined.

III. STABILITY OF GRID-TIED VSCS

Without compromising the small-signal analysis, it shall be assumed that the controller directly outputs the reference voltage v_r, which is delayed by τ_D and then applied as the VSC output v_o. This controller is still labeled as G_c, however it does not feature scaling with the input voltage, unlike $G_c(z)$ in Fig. 1. The analyzed system is modeled without any resistances, which represents the worst case regarding stability, as any resistance positively impacts the system resonance damping [17]. The analysis is performed in the s-domain, to be able to use the model even above the Nyquist frequency, which is shown to be relevant for some cases [5], [12]. In this article, analytics and experimental verifications are given for a two-level single-phase VSC with an inductive filter, as per Fig. 1.

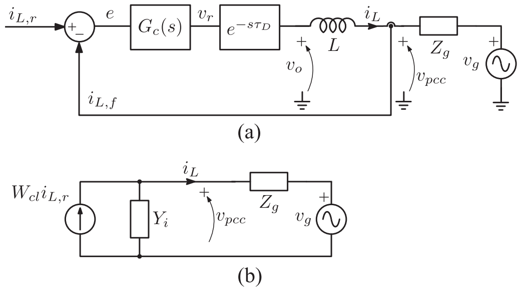

Fig. 3. Grid-connected VSC representation in s-domain. (a) Schematic representing the effects of closed-loop current control and grid voltage on the inductor current. (b) Norton equivalent circuit used for impedance-based stability analysis.

A. Impedance-Based Approach

The impact of closed-loop system and grid voltage on the inductor current can be analyzed using the schematic in Fig. 3(a), given for a system without a feedback filter. The inductor current can be found as a superposition of responses to the imposed reference $i_{L,r}$ and the disturbance v_{pcc}

$$i_L = \frac{1}{sL}\left(v_o - v_{\text{pcc}}\right) = W_{\text{cl}}(s)i_{L,r}(s) - \frac{\frac{1}{sL}}{1+W_{\text{ol}}(s)}v_{\text{pcc}}(s) \tag{3}$$

where L is the filter inductance, $W_{\text{ol}} = \frac{1}{sL}G_c(s)e^{-s\tau_D}$ is the open-loop transfer function, and $W_{\text{cl}}(s) = \frac{W_{\text{ol}}(s)}{1+W_{\text{ol}}(s)}$ is the closed-loop transfer function of the current-controlled system with $Z_g = 0$. The impedance-based stability analysis consists of representing the current-controlled VSC using its Norton equivalent circuit, as shown in Fig. 3(b) [8]. The Norton admittance, referred to as the VSC input admittance $Y_i(s)$, determines the response of inductor current to v_{pcc} when $i_{L,r} = 0$; hence, from (3), it is equal to

$$Y_i(s) = -\frac{i_L}{v_{\text{pcc}}} = \frac{\frac{1}{sL}}{1+\frac{1}{sL}G_c(s)e^{-s\tau_D}}. \tag{4}$$

From (4), it is clear that the input admittance, seen from PCC, depends on the physical VSC output filter and the loop gain of the current-controlled system. At high frequencies, above the control bandwidth, where $|W_{\text{ol}}(s)| \approx 0$, it converges to the physical filter admittance. The impact of the grid impedance Z_g is obtained by substituting $v_{\text{pcc}} = v_g + Z_g i_L$ in (3)

$$i_L(s) = \frac{W_{\text{cl}}(s)}{1+Y_i(s)Z_g(s)}i_{L,r}(s) - \frac{Y_i(s)}{1+Y_i(s)Z_g(s)}v_g(s). \tag{5}$$

Assuming that W_{cl} is stable, the stability of the grid-connected VSC depends on the product $Y_i(s)Z_g(s)$, which is referred to as the minor-loop gain [16]. The system stability can be examined by applying the Nyquist stability criterion to the minor-loop gain.

B. Passivity Criterion

A linear SISO system, such as $Y_i(s)$, is said to be passive if the real part of its frequency response is nonnegative for all frequencies [16]. In other words, $Y_i(s)$ is passive if its phase is limited in the range $[-\frac{\pi}{2}, \frac{\pi}{2}]$. A stronger condition of "strict" passivity is obtained by limiting the phase to the open interval $(-\frac{\pi}{2}, \frac{\pi}{2})$. In case both $Y_i(s)$ and $Z_g(s)$ are passive, the minor-loop gain always satisfies the Nyquist stability criterion as its phase is limited in the range $[-\pi, \pi]$. Imposing the requirement[2] for passive behavior of $Y_i(s)$, as in [18], comes from the fact that a sufficient condition for the VSC stability is satisfied if $Y_i(s)$ is passive and the VSC is connected to another passive network.

C. Controller Design

In this article, single-stage current control loop is implemented, as the focus is on obtaining the passivity inherently, without any AD technique. To achieve good sinusoidal reference tracking and speed of response, a proportional–resonant (PR) controller is used in this article [6]

$$G_c(s) = k_p + k_r\frac{s}{s^2+\omega_1^2} \tag{6}$$

where k_p and k_r are the proportional and resonant gains, respectively, and ω_1 is the angular frequency of the fundamental. The proportional gain is chosen as $k_p = \omega_c L$, where ω_c is the designed angular crossover frequency of the current loop [6]. The resonant gain k_r is chosen so as to have a negligible impact at the crossover frequency [6], $k_r = \frac{1}{10}\omega_c k_p$. The current loop bandwidth, relative to the angular switching frequency ω_{pwm}, $\alpha = \frac{\omega_c}{\omega_{\text{pwm}}}$ can be chosen based on required stability margins, which depend on the total time delay [6]. For single-update ($N = 1$) and double-update ($N = 2$), the crossover frequency is often limited under 10% of the sampling frequency [14], [16]. In case of MS-PWM, the maximum value of α is limited by the switching frequency due to the presence of the switching ripple in m [29].

D. Passivity Measure

In this article, the input feed-forward passivity (IFP) index is used as a measure of the VSC passivity [16], [17]. It is defined as the minimum value of the real part of input admittance, i.e., minimum value of input conductance

$$\text{IFP}(\text{Y}_\text{i}) = \min_{\omega\in\mathbb{R}}\text{Re}\{Y_i\{j\omega\}\} \tag{7}$$

where ω is the angular frequency. The IFP is useful to quantify the impact a VSC may have on the grid stability, as it points to the minimal damping introduced by it. The IFP is negative in case of a nonpassive input admittance.

For a purely proportional controller, the real part of $Y_i(j\omega)$ is calculated using (4)

$$\text{Re}\{Y_i\left(j\omega\right)\}_{k_r=0} = \frac{\omega_c}{L}\frac{\cos\left(\omega\tau_D\right)}{\left(\omega_c - \omega\sin\left(\omega\tau_D\right)\right)^2 + \left(\omega\cos\left(\omega\tau_D\right)\right)^2}. \tag{8}$$

---

[2] In [18], passivity requirement is set above fifth harmonic of the fundamental. Low-frequency passivity issues, e.g., caused by dynamics of the PLL, are not investigated in this article. Since the PLL bandwidth is always set considerably lower than the one of the current loops, its impact on Y_i in medium- and high-frequency range is negligible [4]; hence, it is not included in the admittance model.

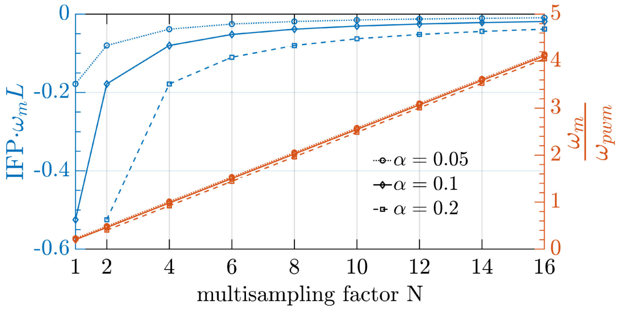

Fig. 4. Left axis shows relative passivity index of the VSC input admittance for proportional controller and three different values of the relative crossover frequency α. Right axis shows frequency for which IFP is found, relative to the switching frequency.

The expression is not given for the case of a PR controller, as it is more complicated and lacks a clear qualitative insight. Nonetheless, the resonant gain is designed such that its impact at high frequencies is very small, meaning that IFP for a PR controller will show a very similar behavior to the one obtained with proportional controller [16]. It can be seen from (8) that, for the proportional controller, the sign of the conductance depends only on the cosine term, whereas its magnitude depends also on bandwidth and is inversely proportional to the value of inductance. The conductance first becomes negative when the argument of the cosine term goes over $\frac{\pi}{2}$. Considering the total time delay in (2), this occurs at the frequency $\frac{N f_{\text{pwm}}}{6}$, which is often referred to as the critical frequency [16]. For the case of single update, nonpassive region is found above $\frac{f_{\text{pwm}}}{6}$, for double update above $\frac{f_{\text{pwm}}}{3}$, etc. It can be concluded that, for the case of naturally sampled PWM, admittance is inherently passive at high frequencies.

To illustrate the impact of system parameters on passivity, IFP for (8) is calculated and shown in Fig. 4. The values are given for different multisampling factors and three values of α, corresponding to $\frac{\omega_c}{\omega_{\text{pwm}}} = \{5, 10, 20\}\%$. For $N = 1$, results are not shown for $\alpha = 0.2$ as such gain results in instability of $W_{\text{cl}}(s)$ in (3). For better generality, values on the left axis show the IFP relative to the VSC filter susceptance at angular frequency ω_m, for which the IFP is found. In this way, results become independent on the specific value of L. On the right axis, values of ω_m are shown. First, it can be seen that control loops with high bandwidths bring significantly stronger negative damping, whereas the frequency at which the IFP is found remains practically constant. This yields the conclusion that passivity issues are more likely to be found in high-bandwidth systems. Second, as the value of N is increased, the relative IFP rapidly converges toward 0. Additionally, ω_m moves to higher frequencies meaning that the absolute IFP, i.e., negative conductance, reduces even more. Finally, it can be concluded that lower values of L result in stronger negative damping. As mentioned, repeating the aforementioned analysis for realistic values of k_r practically does not change results shown in Fig. 4.

There is an ambiguity regarding the interpretation of standards, such as in [18], to determine the upper frequency limit for passivity measurements. Several publications have shown that, for single- and double-update PWM, investigation is necessary also above the Nyquist frequency due to aliasing and side-band PWM components [5], [12]. In [15], authors conclude that if an *LCL* filter is used, even in case the inner current loop is nonpassive, high-frequency components on the grid side flow mainly through the capacitor; hence, the nonpassive high-frequency region of the inner current loop gets compensated and the passivity should only be addressed around the bandwidth. However, it should be noted that the existence of an *LCL* filter can only reduce, and not completely remove, the nonpassive behavior. This is due to the fact that a parallel connection of a nonpassive element and a reactive element remains nonpassive [16]. Generalized conclusion is hard to be brought, as it depends on control bandwidth, passive component sizing, and losses in the circuit. As for the MS-PWM, results shown in Fig. 4 predict the existence of small negative conductances at frequencies significantly above the switching frequency. However, this comes from the small-signal modeling, which does not take into account the PWM nature. Namely, a two-level converter still physically reacts to disturbances only twice per switching period, by modifying rising and falling edges of $x(t)$. This means that it is not likely that a VSC can be active at, for instance, $f = 4f_{\text{pwm}}$. Additionally, for high values of N, small-signal analysis predicts the existence of negative conductances with values very close to 0; hence, even extremely small resistances would be enough to compensate and make the experimental measurements of nonpassive zones impossible. In the end, given that, at frequencies significantly above the bandwidth, the admittance magnitude is determined by the physical VSC output filter, its low-pass nature would require extremely high values of perturbation voltages to cause the resulting current to even be detectable by an ADC. Therefore, subsequent admittance measurements are performed up to $1.5f_{\text{pwm}}$, which is above the Nyquist frequency for the double-update case.

IV. EXPERIMENTAL VERIFICATION

In this section, results of experimental measurements are given to show that the MS-PWM is capable of rendering the admittance passive in a wide frequency range, without any AD. Subsequently, VSC operation in a grid-connected scenario is shown to demonstrate the improved resonance damping obtained using MS-PWM.

For experimental verification, an industrial full-bridge single-phase VSC is used. Two inductive filters with different values of L are used to demonstrate the impact of inductance on the IFP, as seen in Fig. 4. The switching frequency is chosen based on the used IGBTs and the inductor cores. The hardware parameters are shown in Table I. The dead time is set to 1% and the VSC is operated using the bipolar modulation. For input voltage, regenerative power system Keysight RP7962A is used. A photo of the experimental setup is shown in Fig. 5.

The control system is implemented on an NI sbRIO-9606, which is based on a Xilinix Zynq 7020 all programmable system on chip. The inductor current is sensed by a custom interfacing board, based on a shunt resistor. The board uses conditioning

TABLE I
VSC PARAMETERS

Description	label	value	unit
Nominal power	P_n	3	kW
Nominal input voltage	V_{in}	400	V
Nominal PCC voltage	$v_{pcc,RMS}$	230	V
Fundamental frequency	f_1	50	Hz
Switching frequency	f_{pwm}	20	kHz
Filter inductance	L	$\{1.5, 2.5\}$	mH

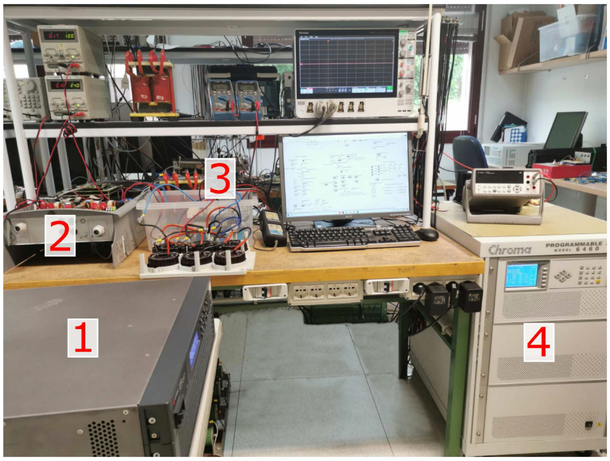

Fig. 5. Experimental setup. 1) Input power supply. 2) VSC and control board. 3) PCC and additional filters used to form resonances or inject perturbations. 4) Programmable ac source.

circuits, a 12-b ADC module AD9226 by Analog Devices, and digital isolators. The DPWM clock runs at 160 MHz.

For the digital implementation of (6), used in subsequent experimental tests, the controller is discretized using the impulse-invariant approach [6]

$$G_c(z) = k_p + k_r T_s \frac{1 - \cos(\omega_1 T_s) z^{-1}}{1 - 2\cos(\omega_1 T_s) z^{-1} + z^{-2}}. \quad (9)$$

The results are given for values of $N \in \{2, 4, 8, 16, 32\}$.

A. Admittance Measurements

Admittance measurements of current-controlled converters are typically performed by setting the current reference to 0, which disconnects the Norton current source shown in Fig. 3(b) [12], [15]. The perturbation voltage is applied to the converter output filter and the measured admittance determines the current response. The dc current reference requires no synchronization with the PCC voltage. Note that even if nonzero grid-frequency ac current reference is imposed, PLL bandwidth must be set well-below the current loop bandwidth [9]; hence, its impact can always be considered negligible for high-frequency passivity properties [4].

The circuit used for admittance measurements, as shown in Fig. 6, consists of the tested VSC, the perturbation branch, and the bias branch. The perturbation source v_p is implemented using a power operational amplifier PA107DP, from APEX. Due to the current limit of PA107DP, the admittance measurements are conducted for lowered value of $V_{\text{in}} = 250$ V and for the higher inductance $L = 2.5$ mH, so that the switching ripple of i_L is decreased. The value of V_{in} does not impact the small-signal admittance, as seen in (4). The perturbation source is connected in series with a capacitor $C_p = 10\ \mu$F and a resistor $R_p = 1\ \Omega$ that is used to smooth any transients. The capacitor is used to block dc currents as well as to decouple the bias branch from the VSC, so that switching ripple harmonics of i_L remain the same as if VSC was connected to an ideal grid. In this way, conclusions obtained through verification of the impact of MS-PWM nonlinearities on admittance measurements remain valid for grid-connected operation [36]. The bias branch features an inductance $L_b = 2.4$ mH, which suppresses perturbation currents, and a resistor R_b that can be bypassed with a switch s_b. The bias branch has two functions. First of all, it allows the circulation of any dc current. All admittance measurements are performed for an imposed dc current reference, such that no current crossover occurs. This scenario is more critical as it is reported that dead times may provide certain damping when current crosses 0 [49]. Note that a dc component of i_L does not impact admittance measurements in the high-frequency range. Second, when the switch s_b is opened, dc component of i_L provides a voltage drop across R_b. This results in a dc voltage component of v_{pcc}, referred to as the bias voltage v_b. By imposing the adequate bias voltage, it is possible to obtain admittance measurements around specific operating points. As the PWM itself is nonlinear, and to some extent operating point dependent [28], investigation of small-signal properties of the system makes sense to be performed only around stable and constant operating points. When the converter operates connected to an ac grid, its operating point moves in a certain range and the measured admittance is expected to be some sort of average of the results obtained for steady operating points in the same range. Measurements for constant operating points also allow the investigation of MS-PWM nonlinearities impact on admittance. Admittances are measured without, and for three positive values of voltage bias. For bias values of 65 and 75 V, the resistance is set to $R_b = 24\ \Omega$. For 150-V bias, the resistance is set to $R_b = 48\ \Omega$. These bias values determine the steady-state operating point as $D = 0.5(\frac{v_b}{V_{\text{in}}} + 1)$, if series voltage drops are neglected.

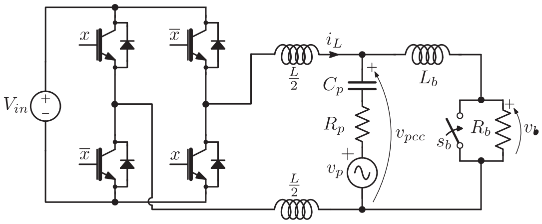

Fig. 6. Circuit used for admittance measurements.

The admittance is measured for 17 frequencies, one at the time, in the range from 5 to 31.5 kHz ($0.25 f_{\text{pwm}}$ to $1.575 f_{\text{pwm}}$), avoiding the switching frequency. For each point, a sinusoidal

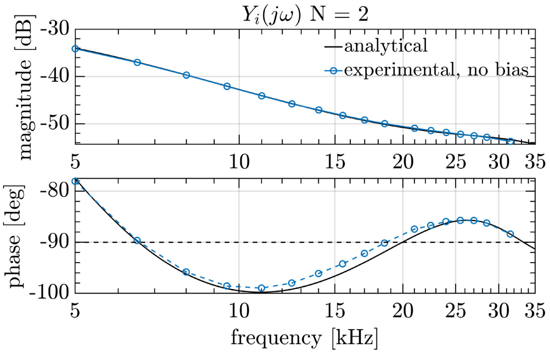

Fig. 7. Admittance measurements for $L = 2.5$ mH, $N = 2$, and $\alpha = 0.1$, without dc bias.

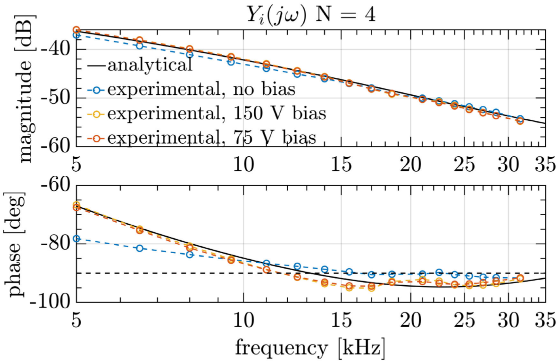

Fig. 8. Admittance measurements for $L = 2.5$ mH, $N = 4$, $\alpha = 0.1$, and three values of dc bias. Without dc bias, vertical crossings between m and w occur.

v_p with perturbation frequency f_p is imposed. Its magnitude is calculated to obtain at least 100-mA magnitude of perturbation current component flowing through the VSC. This allows precise measurements using the oscilloscope, in the presence of switching ripple and noise. The inductor current i_L and the output voltage v_{pcc} are acquired through the oscilloscope with data length of 20 ms. This yields a spectral resolution, relative to the perturbation frequency, of 1 % for $f_p = 5$ kHz, which further improves as f_p is increased. The data are postprocessed in MATLAB, by calculating the FFT of $-i_L$ and v_{pcc}. Based on magnitude ratio of perturbation components, and their phase difference, admittance at f_p is calculated. The measurements are performed for the relative crossover frequency $\alpha = 0.1$. The results are compared with the analytical model, calculated as the frequency response of (4).

As a benchmark, the admittance is measured for double-update control. Given that MS-PWM nonlinearities are not present for $N = 2$ [36], results in Fig. 7 are shown only for the case without bias voltage. First of all, it can be seen that an excellent match with analytical modeling is achieved, even above the Nyquist frequency. This justifies the validity of s-domain modeling. A nonpassive zone starts from 6.5 kHz, which matches with the double-update critical frequency obtained for a proportional controller, $\frac{f_{\text{pwm}}}{3}$. Analytical admittance predicts another nonpassive zone above 34 kHz, which is outside of the measurement range.

Results for $N = 4$ are given in Fig. 8, without bias and for bias levels of 75 and 150 V. Without bias voltage, duty cycle is perturbed around a steady-state value of $D = 0.5$. It can be seen that for that case, measurements show a slight mismatch from analytics, particularly in the range below 10 kHz. It is verified that, for this operating point, one edge of x is determined by a vertical crossing between m and w, which results in reduced-gain operation [36]. It is interesting to note that, at higher frequencies, this nonlinearity does not cause the admittance to go deeper in the nonpassive zone; on the contrary, it seems that this operation adds some damping to the system. The same effect is noticed for other values of N under reduced-gain operation. In Fig. 8, when dc bias is added, the operating point is such that no vertical crossings occur, and a good match with analytics is seen. Around 12 kHz, the admittance enters the nonpassive zone, however, this zone is much less emphasized compared to $N = 2$.

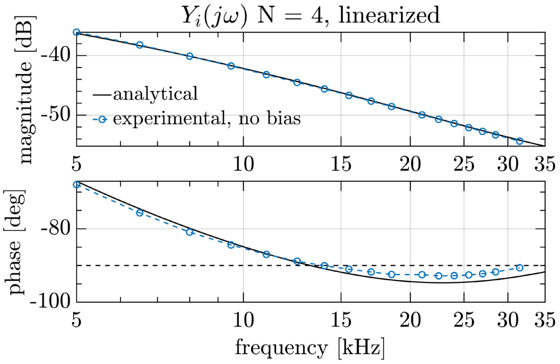

Fig. 9. Admittance measurements for $L = 2.5$ mH, $N = 4$, and $\alpha = 0.1$, and no dc bias. MS-PWM is linearized such that no vertical crossings between m and w occur.

It is of interest to verify whether the mismatch for $N = 4$ without bias results from the MS-PWM nonlinearity. Hence, MS-PWM behavior is linearized, using the approach from the work in [36]. In that article, it is shown that vertical crossings, caused by the switching ripple component of the modulating waveform, can be completely removed for $N = 4$, by adding a low-pass filter with a suitable cutoff frequency to the feedback path. For the specific case, this is designed as a first-order filter with a cutoff frequency of 39 kHz, discretized using Bilinear transform. The filter's impact is solely on shifting the switching ripple component, with respect to the carrier, in order to prevent vertical crossings, and its impact on dynamics is negligible. The corresponding results are shown in Fig. 9, and it can be seen that a good match with analytics is now obtained. This confirms that the effect observed in Fig. 8 is due to MS-PWM nonlinearities.

Results for $N = 8$ are given in Fig. 10 and similar conclusions as for $N = 4$ can be brought. Analytics predict that for $N = 8$, nonpassive zone occurs around 26 kHz, with the phase of Y_i being just slightly under $-\frac{\pi}{2}$. As for $N = 4$, without bias, the reduced-gain operation is present and mismatch from analytics is seen. Again, this mismatch is more evident at lower frequencies, and no detrimental impact on passivity occurs. Note that some

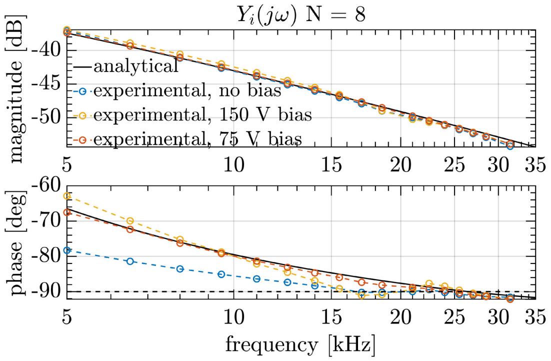

Fig. 10. Admittance measurements for $L = 2.5$ mH, $N = 8$, and $\alpha = 0.1$, and three values of dc bias. Without dc bias, vertical crossings between m and w occur.

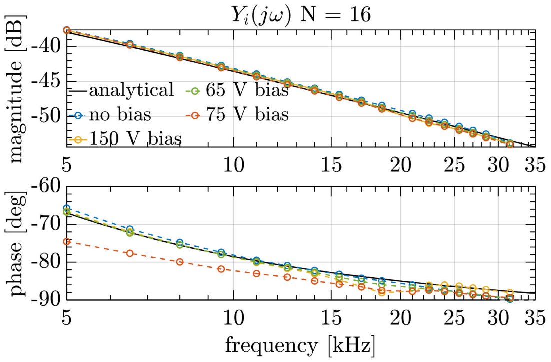

Fig. 11. Admittance measurements for $L = 2.5$ mH, $N = 16$, and $\alpha = 0.1$, and four values of dc bias. For 75-V bias, vertical crossings between m and w occur. Word "experimental" is omitted from the legend to fit the figure.

drop in phase is seen with 150-V bias at frequencies very close to the switching frequency. This effect is also measured for other oversampling factors, including $N = 2$, hence it is not ascribed to the MS-PWM behavior. At frequencies very close to f_{pwm}, precise information on admittance and especially on its phase is hard to obtain, as many nonlinear effects, such as PWM sidebands and aliasing, may interfere [5], [12], [27], [39]–[42]. These drops were also noticed in simulations, which were performed to verify the consistency of measurements.

Results for $N = 16$ are given in Fig. 11. For 75-V bias, reduced-gain operation is present. Results are also shown for 65-V bias, which slightly moves the operating point, enough to prevent vertical crossings between m and w, yielding again a very good match with analytics. The measurements show that, for all tested operating points, admittance does not enter the nonpassive zone. Moreover, the admittance is strictly passive, which indicates additional robustness. Results for $N = 32$ are given in Fig. 12. For all operating points, match with analytics is excellent and the admittance is strictly passive.

For a comparison, Fig. 13 is given to show real parts of measured admittances for all tested values of N. A clear improvement of passivity is obtained as N is increased. The results are given for operating points that do not feature emphasized impact of MS-PWM nonlinearities.

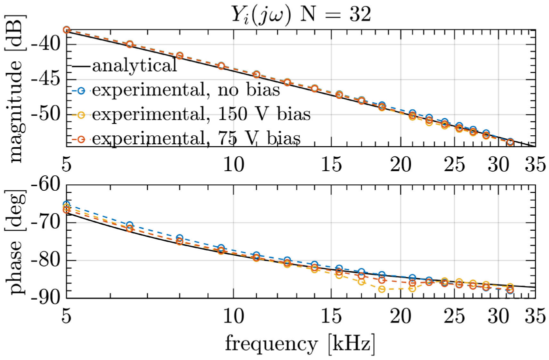

Fig. 12. Admittance measurements for $L = 2.5$ mH, $N = 32$, and $\alpha = 0.1$, and three values of dc bias.

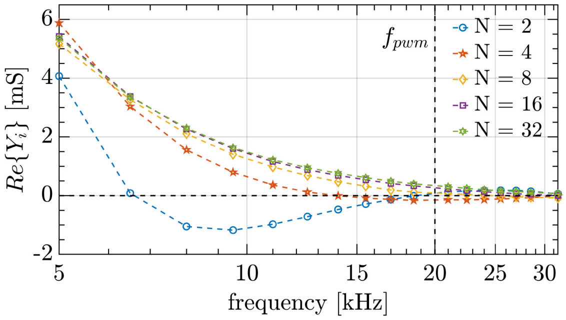

Fig. 13. Comparison of real parts of experimentally measured admittances for all tested values of N, $L = 2.5$ mH, and $\alpha = 0.1$.

Experimental admittance measurements were not performed while the VSC was connected to a sinusoidal ac source with the frequency f_1. This kind of setup would perturb the operating point with the frequency f_1, which would not be consistent with small-signal analysis of an inherently nonlinear system. However, it should be noted that simulations were performed for such case, as required by standard [18], and the impact of MS-PWM nonlinearities was not seen; the measurements still matched well with analytical modeling and all passivity-related conclusions remain valid. The results were somewhere in between results for tested dc operating points that did not feature vertical crossings between m and w. This leads to the conclusion that, regarding passivity, effects of MS-PWM nonlinearities, which arise at specific operating points, may be masked by the ac operation. However, a general conclusion for any fundamental frequency and perturbation magnitude cannot be brought. The simulation results are not shown for the sake of paper conciseness.

It should be stated that the experimental results show a very good match with analytics, with errors in the range of a few degrees. This confirms the validity of used DPWM modeling in (1). In [12], where a more complex multifrequency modeling procedure is presented, some mismatch is present both in phase and magnitude. The experimental measurements in [12] are performed up to the switching frequency, for single-update case. In [15], measurements are performed slightly above the Nyquist frequency, for single-update case, and a higher mismatch from analytical modeling is seen compared to results of this article.

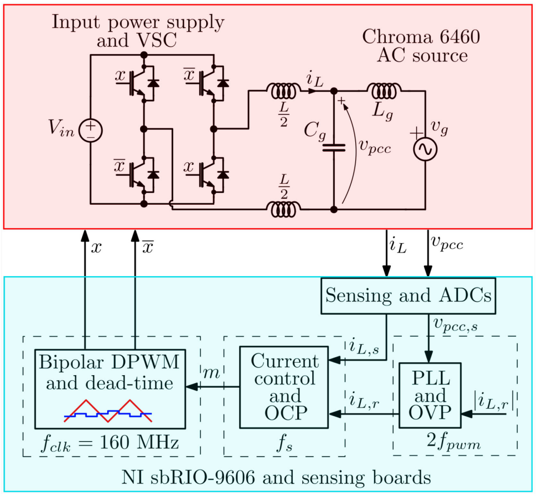

Fig. 14. Illustration of a grid-connected scenario. Grid resonance appears due to the presence of C_g and L_g. In blue part, OCP and OVP stand for overcurrent and overvoltage protection, respectively.

This can be partly due to the use of z-domain modeling in [15], which fails around the Nyquist frequency.

To conclude, the results of this section have shown that MS-PWM is capable of rendering the admittance strictly passive in a wide frequency range, which provides compliance with the standard [18] without any AD. Some impact of MS-PWM nonlinearities is present; however, its nature is not found to be detrimental for passivity properties.

B. Grid-Connected Operation

The objective of this section is to show the implication of connecting a VSC with a nonpassive input admittance to a grid with a resonance that falls into the nonpassive region. The VSC works as a rectifier with a unity power factor, output frequency is $f_1 = 50$ Hz, and the PLL is implemented with 5-Hz bandwidth. The schematic of the grid-connected scenario is shown in Fig. 14.

Operation is tested for $N = \{2, 4, 32\}$, two values of the relative crossover frequency $\alpha = 0.2$ and $\alpha = 0.1$, and two values of filter inductance, $L = 1.5$ mH and $L = 2.5$ mH. The two inductors feature the same core properties and similar winding resistances, yielding comparable losses. The values of passive components are $C_g = 6.7\ \mu$F and $L_g = 72\ \mu$H. The grid voltage is formed using Chroma 6460 programmable ac source. Due to unknown high-frequency damping properties of the ac source, it was of interest to decouple it from the resonant circuit. This was achieved by connecting Chroma via an *LC* filter with inductance $L_{ch} = 324\ \mu$H and $C_{ch} = 150\ \mu$F. In this way, an almost ideal ac source, at the frequencies of interest, was formed. This source is shown in Fig. 14 as v_g. With such a configuration of reactive elements, two resonant frequencies appear in the circuit. The first one, due to decoupling of the ac source, is found close to 650 Hz and it has no direct implications on passivity tests. The second one appears at $f_{\text{res}} = 7.63$ kHz, which is very close to the frequency where IFP is found for $N = 2$. For other tested values of N, MS-PWM renders the admittance passive around f_{res}. Relatively high Q factor of the resonant circuit was verified by triggering transients while the VSC was disconnected. To illustrate the impact of the values of inductance and bandwidth on the negative damping introduced by the VSC when $N = 2$, Fig. 15 shows the real part of Y_i for tested values of L and α. The small-signal modeling predicts that the case with higher bandwidth and lower inductance will have the worst impact on stability.

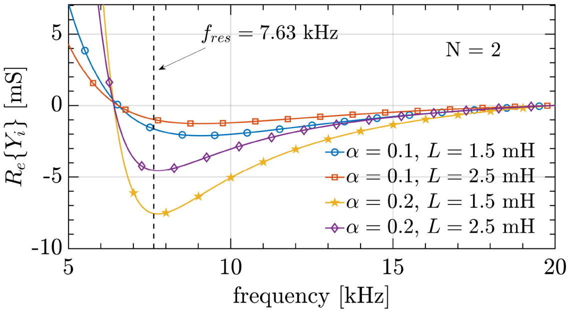

Fig. 15. Real part of the VSC input admittance Y_i for double-update control, two tested inductances L, and two tested relative bandwidths α.

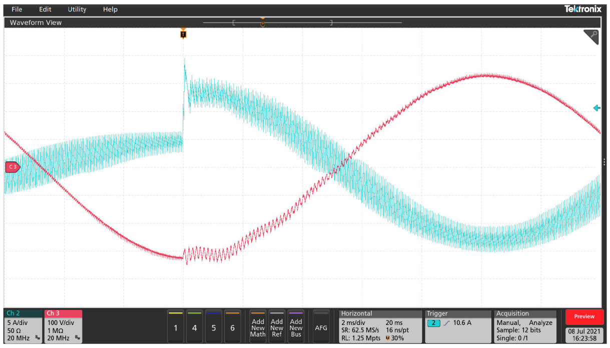

Ch 2
5 A/div
50 Ω
20 MHz

Ch 3
100 V/div
1 MΩ
20 MHz

Horizontal
2 ms/div 20 ms
SR: 62.5 MS/s 16 ns/pt
RL: 1.25 Mpts 30%

Trigger
2 10.6 A

Acquisition
Manual, Analyze
Sample: 12 bits
Single: 0 /1

08 Jul 2021
16:23:58

Fig. 16. Experimental tests of a grid-connected scenario. Reference current magnitude is changed from 4 to 12 A. System parameters are: $N = 2$, $\alpha = 0.2$, $L = 1.5$ mH, $V_{\text{in}} = 400$ V, and $v_{\text{pcc,rms}} = 230$ V.

The experimental results show oscilloscope measurements of one fundamental period of i_L (blue trace) and v_{pcc} (red trace). To test the impact of various system parameters on total damping, results are also given for two settings of input/output voltages: $V_{\text{in}} = 400$ V and $v_{\text{pcc,RMS}} = 230$ V, and $V_{\text{in}} = 250$ V and $v_{\text{pcc,RMS}} = 110$ V. Current magnitude reference features a step change from 4 to 12 A. The reference change is synchronized with the instant where current is at its peak value, in order to trigger a strong transient.

In Fig. 16, results are shown for the case of $N = 2$, $\alpha = 0.2$, $L = 1.5$ mH, $V_{\text{in}} = 400$ V, and $v_{\text{pcc,rms}} = 230$ V. For all tested cases of $N = 2$ and $\alpha = 0.2$, phase margin is relatively low, around 30 °, which can be seen from the step response overshoot. Note that the same relative bandwidth is used in experimental results in [14] and a slightly higher one is used in [15]. When reference step change is imposed, oscillations at resonant frequency are evident, especially on the v_{pcc} trace. After nearly half fundamental period, oscillations are fully damped due to

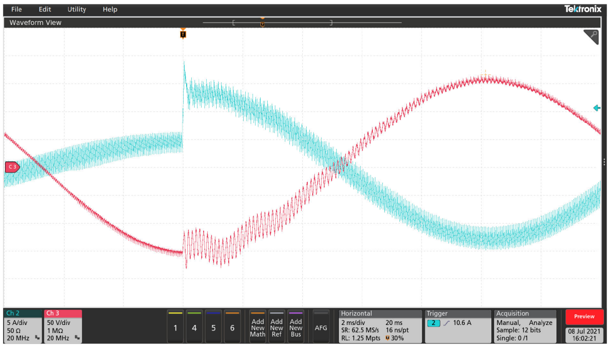

Fig. 17. Experimental tests of a grid-connected scenario. Reference current magnitude is changed from 4 to 12 A. System parameters are: $N = 2$, $\alpha = 0.2$, $L = 1.5$ mH, $V_{\text{in}} = 250$ V, and $v_{\text{pcc,rms}} = 110$ V.

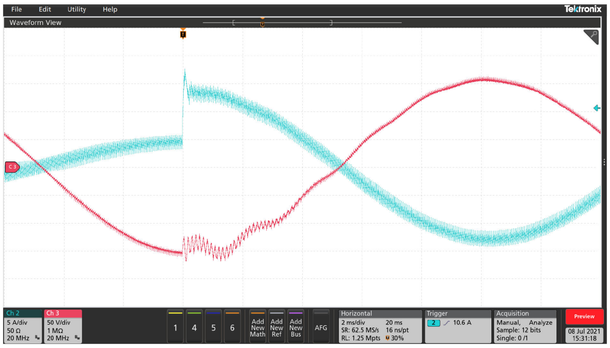

Fig. 18. Experimental tests of a grid-connected scenario. Reference current magnitude is changed from 4 to 12 A. The control system parameters are: $N = 2$, $\alpha = 0.2$, $L = 2.5$ mH, $V_{\text{in}} = 250$ V, and $v_{\text{pcc,rms}} = 110$ V.

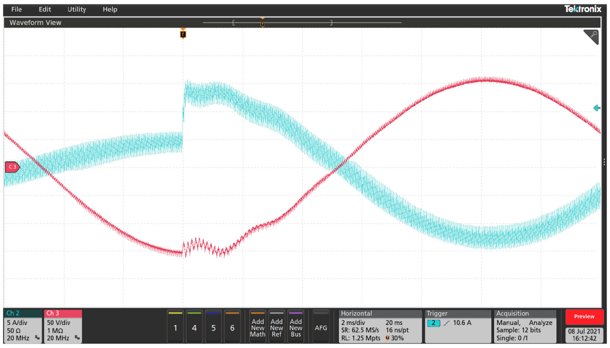

Fig. 19. Experimental tests of a grid-connected scenario. Reference current magnitude is changed from 4 to 12 A. System parameters are: $N = 2$, $\alpha = 0.1$, $L = 1.5$ mH, $V_{\text{in}} = 250$ V, and $v_{\text{pcc,rms}} = 110$ V.

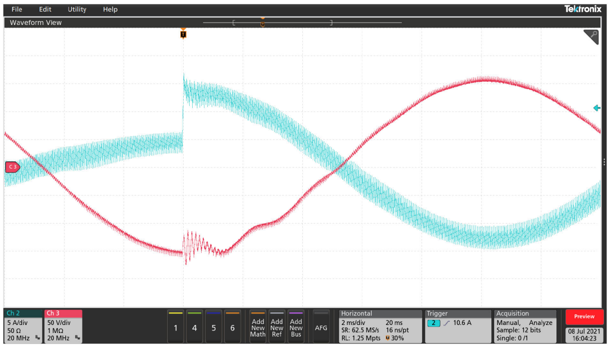

Fig. 20. Experimental tests of a grid-connected scenario. Reference current magnitude is changed from 4 to 12 A. System parameters are: $N = 4$, $\alpha = 0.2$, $L = 1.5$ mH, $V_{\text{in}} = 250$ V, and $v_{\text{pcc,rms}} = 110$ V.

nonnegligible passive damping of the grid resonant circuit. Note the additional presence of lower frequency oscillations, corresponding to the above-mentioned ac source decoupling.

For the subsequent test, as shown in Fig. 17, control remains double-update with $\alpha = 0.2$ and $L = 1.5$ mH. However, the voltages are changed to $V_{\text{in}} = 250$ V, and $v_{\text{pcc,rms}} = 110$ V. Much stronger oscillations can be seen, but again, resistances of the experimental resonant circuit do not allow the full system instability to occur. It is very important to note that, based on small-signal modeling, lowering the input/output voltages does not have any impact on passivity. Most likely, higher passive damping is introduced with $V_{\text{in}} = 400$ V due to the larger current ripple, which causes more losses in the circuit. For all subsequent tests, $V_{\text{in}} = 250$ V and $v_{\text{pcc,rms}} = 110$ V are chosen to enable a more critical scenario regarding stability.

In Fig. 18, results are shown for the case of higher inductance: $N = 2$, $\alpha = 0.2$, $L = 2.5$ mH, $V_{\text{in}} = 250$ V, and $v_{\text{pcc,rms}} = 110$ V. It can be seen that much stronger resonance damping is present than in Fig. 17. Since the two cases feature the same crossover frequency and phase margin, the only difference in damping comes from better passivity measures of VSCs with higher values of L, as predicted by Fig. 15.

To show the impact of reducing the bandwidth, in Fig. 19, results are shown for the case of $N = 2$, $\alpha = 0.1$, $L = 1.5$ mH, $V_{\text{in}} = 250$ V, and $v_{\text{pcc,rms}} = 110$ V. It can be seen that oscillations are strongly damped compared to the case with the same parameters except for a higher α, seen in Fig. 17.

To verify the positive impact of MS-PWM on damping, control systems with $N = 4$ and $N = 32$ were tested for the most critical system parameters: $\alpha = 0.2$, $L = 1.5$ mH, $V_{\text{in}} = 250$ V, and $v_{\text{pcc,rms}} = 110$ V. The results are directly comparable to the one seen in Fig. 17. For $N = 4$, results are shown in Fig. 20. It can be seen that, compared to double-update case, resonant oscillations are fully damped in significantly less time. For $N = 32$, results are shown in Fig. 21 and it is clear that the damping is even higher.

The experimental results are consistent with the analytical prediction of the impact of N, L, and α on the introduced negative damping. In our experimental setup, transients trigger oscillations at the resonant frequency; however, full system instability does not occur. This confirms that passivity is not a necessary condition for the system stability, as damped grid resonances can compensate the nonpassive input admittance of the VSC.

Two positive aspects of MS-PWM are seen from the presented results. First, due to delay reduction, for the same crossover frequency, phase margin is improved compared to $N = 2$, which can be seen from the step response. Second, MS-PWM renders the admittance passive, which results in high damping of oscillations at resonant frequency. Therefore, MS-PWM offers the

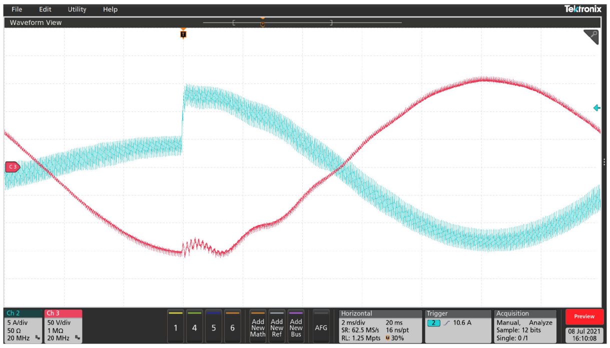

Ch 2
5 A/div
50 Ω
20 MHz

Ch 3
50 V/div
1 MΩ
20 MHz

Horizontal
2 ms/div 20 ms
SR: 62.5 MS/s 16 ns/pt
RL: 1.25 Mpts 30%

Trigger
2 10.6 A

Acquisition
Manual, Analyze
Sample: 12 bits
Single: 0 /1

08 Jul 2021
16:10:08

Fig. 21. Experimental tests of a grid-connected scenario. Reference current magnitude is changed from 4 to 12 A. System parameters are: $N = 32, \alpha = 0.2$, $L = 1.5$ mH, $V_{\text{in}} = 250$ V, and $v_{\text{pcc,rms}} = 110$ V.

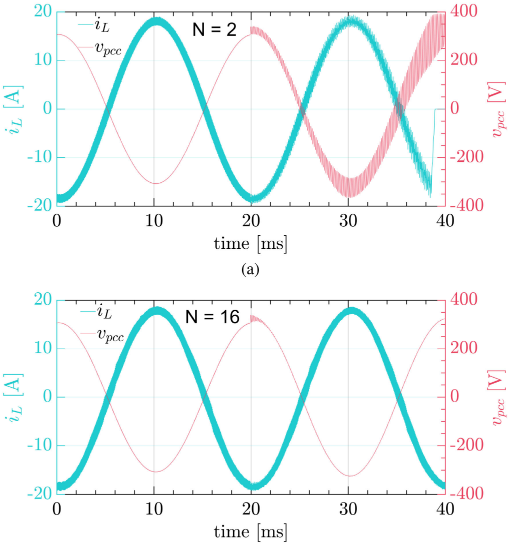

(a)

(b)

Fig. 22. HIL tests of a grid-connected scenario. 1-Ω resistance, placed in series with L_g, is paralleled with a 50-mΩ resistor at $t = 20$ ms. System parameters are: $\alpha = 0.2, L = 2.5$ mH, $V_{\text{in}} = 400$ V, $v_{\text{pcc,rms}} = 230$ V, and: (a) $N = 2$ and (b) $N = 16$.

capability of implementing very high bandwidth loops, whereas the passivity extension is inherently provided, without any additional AD strategy.

As a final verification, hardware-in-th\e-loop (HIL) results are given to demonstrate the instability condition in case the VSC is connected to a grid resonance with a very high-quality factor. These results were not obtainable in our experimental setup; however, in a general case, the grid resonance can feature very low passive damping. The simulations were organized using the Typhoon HIL 402 HIL platform to emulate the VSC and the grid, i.e., red part in Fig. 14. The inductor current and the PCC voltage are obtained via HIL analog outputs. Sensing, ADC, PLL, current control, and modulation were implemented on the same control platform that was used in experimental tests, i.e., blue part in Fig. 14 remains unchanged, except for input signal scaling. Resulting transistor switching signals are connected to HIL digital inputs. In order to verify the consistency of the simulation, all admittance measurements were repeated and results matched those obtained experimentally; hence, admittance properties remain unchanged. These results are not shown for the presentation conciseness. For the instability test, operation is compared between $N = 2$ and $N = 16$ and the chosen system parameters are: $\alpha = 0.2, L = 2.5$ mH, $V_{\text{in}} = 400$ V, $v_{\text{pcc,rms}} = 230$ V, and $P = P_n = 3$ kW. 1-Ω resistor is placed in series with the grid inductance L_g. At $t = 20$ ms, the resistor is paralleled with another resistor of 50 $\text{m}\Omega$, in order to reduce the passive damping and observe the transient. The voltage protection is set to turn OFF the VSC at instant when $|v_{\text{pcc}}|$ exceeds 380 V or $|i_L|$ exceeds 25 A. The results are shown in Fig. 22. It can be seen that for $N = 2$, stable operation cannot be maintained as the grid resonance, which falls into the nonpassive admittance region, is no longer damped by the 1-Ω resistor. The protection is triggered at approximately $t = 39$ ms and the VSC is turned OFF. On the other hand, for $N = 16$ and the same exact test, the operation remains stable and resonant oscillations are quickly damped.

V. CONCLUSION

This article has shown that MS-PWM is capable of rendering the VSC admittance passive in a wide frequency range, which provides compliance with the standard [18]. This is achieved without any AD technique, which significantly reduces the system complexity, cost, and sensitivity to noise and parameter mismatch. Some impact of MS-PWM nonlinearities is present; however, it is not found to be detrimental for passivity properties. Even for lower values of N, where the measured admittance still features a small nonpassive zone, resulting negative damping is strongly reduced compared to double update. The MS-PWM is shown to be a promising candidate for grid-connected VSCs as it enables very high bandwidths while inherently suppressing the nonpassive input admittance behavior. To enable highest damping and lowest impact of MS-PWM nonlinearities, it is advisable to choose as high oversampling factor as allowed by the control platform.

REFERENCES

[1] F. Blaabjerg, R. Teodorescu, M. Liserre, and A. Timbus, “Overview of control and grid synchronization for distributed power generation systems,” *IEEE Trans. Ind. Electron.*, vol. 53, no. 5, pp. 1398–1409, Oct. 2006.
[2] D. Boroyevich, I. Cvetkovic, R. Burgos, and D. Dong, “Intergrid: A future electronic energy network?,” *IEEE Trans. Emerg. Sel. Topics Power Electron.*, vol. 1, no. 3, pp. 127–138, Sep. 2013.
[3] X. Wang and F. Blaabjerg, “Harmonic stability in power electronic-based power systems: Concept, modeling, and analysis,” *IEEE Trans. Smart Grid*, vol. 10, no. 3, pp. 2858–2870, May 2019.
[4] L. Harnefors, X. Wang, A. G. Yepes, and F. Blaabjerg, “Passivity-based stability assessment of grid-connected VSCs—An overview,” *IEEE Trans. Emerg. Sel. Topics Power Electron.*, vol. 4, no. 1, pp. 116–125, Mar. 2016.
[5] L. Harnefors, R. Finger, X. Wang, H. Bai, and F. Blaabjerg, “VSC input-admittance modeling and analysis above the Nyquist frequency for passivity-based stability assessment,” *IEEE Trans. Ind. Electron.*, vol. 64, no. 8, pp. 6362–6370, Aug. 2017.
[6] S. Buso and P. Mattavelli, “Digital control in power electronics,” in *Synthesis Lectures on Power Electronics*, 2nd ed. San Rafael, CA, USA: Morgan & Claypool, 2015.
[7] R. D. Middlebrook, “Input filter considerations in design and application of switching regulators,” in *Proc. IEEE Ind. Appl. Soc. Annu. Meeting*, Chicago, IL, USA, October 1976, 366–382.
[8] J. Sun, “Impedance-based stability criterion for grid-connected inverters,” *IEEE Trans. Power Electron.*, vol. 26, no. 11, pp. 3075–3078, Nov. 2011.

[9] B. Wen, D. Dong, D. Boroyevich, R. Burgos, P. Mattavelli, and Z. Shen, "Impedance-based analysis of grid-synchronization stability for three-phase paralleled converters," *IEEE Trans. Power Electron.*, vol. 31, no. 1, pp. 26–38, Jan. 2016.

[10] B. Wen, D. Boroyevich, R. Burgos, P. Mattavelli, and Z. Shen, "Analysis of D-Q small-signal impedance of grid-tied inverters," *IEEE Trans. Power Electron.*, vol. 31, no. 1, pp. 675–687, Jan. 2016.

[11] X. Wang, L. Harnefors, and F. Blaabjerg, "Unified impedance model of grid-connected voltage-source converters," *IEEE Trans. Power Electron.*, vol. 33, no. 2, pp. 1775–1787, Feb. 2018.

[12] F. D. Freijedo, M. Ferrer, and D. Dujic, "Multivariable high-frequency input-admittance of grid-connected converters: Modeling, validation, and implications on stability," *IEEE Trans. Ind. Electron.*, vol. 66, no. 8, pp. 6505–6515, Aug. 2019.

[13] V. Pirsto, J. Kukkola, M. Hinkkanen, and L. Harnefors, "Inter-sample modeling of the converter output admittance," *IEEE Trans. Ind. Electron.*, vol. 68, no. 11, pp. 11348–11358, Nov. 2021.

[14] L. Harnefors, A. G. Yepes, A. Vidal, and J. Doval-Gandoy, "Passivity-based controller design of grid-connected VSCs for prevention of electrical resonance instability," *IEEE Trans. Ind. Electron.*, vol. 62, no. 2, pp. 702–710, Feb. 2015.

[15] E. Rodriguez-Diaz, F. D. Freijedo, J. M. Guerrero, J.-A. Marrero-Sosa, and D. Dujic, "Input-admittance passivity compliance for grid-connected converters with an LCL filter," *IEEE Trans. Ind. Electron.*, vol. 66, no. 2, pp. 1089–1097, Feb. 2019.

[16] F. Hans, W. Schumacher, S.-F. Chou, and X. Wang, "Passivation of current-controlled grid-connected VSCs using passivity indices," *IEEE Trans. Ind. Electron.*, vol. 66, no. 11, pp. 8971–8980, Nov. 2019.

[17] J. Serrano-Delgado, S. Cobreces, M. Rizo, and E. J. Bueno, "Low-order passivity-based robust current control design for grid-tied VSCs," *IEEE Trans. Power Electron.*, vol. 36, no. 10, pp. 11886–11899, Oct. 2021.

[18] *Railway Applications—Power Supply and Rolling Stock—Technical Criteria for the Coordination Between Power Supply (Substation) and Rolling Stock to Achieve Interoperability*, CENELEC Standard EN50388, 2012.

[19] J. Dannehl, M. Liserre, and F. W. Fuchs, "Filter-based active damping of voltage source converters with LCL filter," *IEEE Trans. Ind. Electron.*, vol. 58, no. 8, pp. 3623–3633, Aug. 2011.

[20] X. Wang, F. Blaabjerg, and P. C. Loh, "Passivity-based stability analysis and damping injection for multiparalleled VSCs with LCL filters," *IEEE Trans. Power Electron.*, vol. 32, no. 11, pp. 8922–8935, Nov. 2017.

[21] H. Yu, M. A. Awal, H. Tu, Y. Du, S. Lukic, and I. Husain, "Passivity-oriented discrete-time voltage controller design for grid-forming inverters," in *Proc. IEEE Energy Convers. Congr. Expo.*, 2019, pp. 469–475.

[22] C. Xie, K. Li, J. Zou, and J. M. Guerrero, "Passivity-based stabilization of LCL-type grid-connected inverters via a general admittance model," *IEEE Trans. Power Electron.*, vol. 35, no. 6, pp. 6636–6648, Jun. 2020.

[23] H. Wu and X. Wang, "Virtual-flux-based passivation of current control for grid-connected VSCs," *IEEE Trans. Power Electron.*, vol. 35, no. 12, pp. 12673–12677, Dec. 2020.

[24] Y. Liao, X. Wang, and F. Blaabjerg, "Passivity-based analysis and design of linear voltage controllers for voltage-source converters," *IEEE Open J. Ind. Electron. Soc.*, vol. 1, pp. 114–126, Jun. 2020, doi: 10.1109/OJIES.2020.3001406.

[25] M. A. Awal, L. Della Flora, and I. Husain, "Observer based generalized active damping for voltage source converters with LCL filters," *IEEE Trans. Power Electron.*, vol. 37, no. 1, pp. 125–136, Jan. 2022.

[26] G. Walker, "Digitally-implemented naturally sampled PWM suitable for multilevel converter control," *IEEE Trans. Power Electron.*, vol. 18, no. 6, pp. 1322–1329, Nov. 2003.

[27] L. Corradini and P. Mattavelli, "Modeling of multi-sampled pulse width modulators for digitally controlled DC–DC converters," *IEEE Trans. Power Electron.*, vol. 23, no. 4, pp. 1839–1847, Jul. 2008.

[28] L. Corradini, W. Stefanutti, and P. Mattavelli, "Analysis of multi-sampled current control for active filters," *IEEE Trans. Ind. Appl.*, vol. 44, no. 6, pp. 1785–1794, Nov./Dec. 2008.

[29] R. Gupta, A. Ghosh, and A. Joshi, "Characteristic analysis for multi-sampled digital implementation of fixed-switching-frequency closed-loop modulation of voltage-source inverter," *IEEE Trans. Ind. Electron.*, vol. 56, no. 7, pp. 2382–2392, Jul. 2009.

[30] X. Zhang, P. Chen, C. Yu, F. Li, H. T. Do, and R. Cao, "Study of a current control strategy based on multisampling for high-power grid-connected inverters with an LCL filter," *IEEE Trans. Power Electron.*, vol. 32, no. 7, pp. 5023–5034, Jul. 2017.

[31] J. Ma, X. Wang, F. Blaabjerg, W. Song, S. Wang, and T. Liu, "Multisampling method for single-phase grid-connected cascaded H-bridge inverters," *IEEE Trans. Ind. Electron.*, vol. 67, no. 10, pp. 8322–8334, Oct. 2020.

[32] Z. Zhou, J. Wang, Z. Liu, and J. Liu, "Accurate prediction of vertical crossings for multi-sampled digital-controlled buck converters," in *Proc. IEEE Appl. Power Electron. Conf. Expo.*, 2020, pp. 292–298.

[33] I. Z. Petric, P. Mattavelli, and S. Buso, "A jitter amplification phenomenon in multi-sampled digital control of power converters," *IEEE Trans. Power Electron.*, vol. 36, no. 8, pp. 8685–8695, Aug. 2021.

[34] S. He, D. Zhou, X. Wang, and F. Blaabjerg, "Aliasing suppression of multi-sampled current controlled LCL-filtered inverters," *IEEE Trans. Emerg. Sel. Topics Power Electron.*, to be published, doi: 10.1109/JESTPE.2021.3050886.

[35] I. Z. Petric, P. Mattavelli, and S. Buso, "Feedback noise propagation in multi-sampled DC–DC power electronic converters," *IEEE Trans. Power Electron.*, vol. 37, no. 1, pp. 150–161, Jan. 2022.

[36] I. Z. Petric, P. Mattavelli, and S. Buso, "Investigation of nonlinearities introduced by multi-sampled pulsewidth modulators," *IEEE Trans. Power Electron.*, vol. 37, no. 3, pp. 2538–2550, Mar. 2022.

[37] D. van de Sype, K. De Gusseme, A. van den Bossche, and J. Melkebeek, "Small-signal Laplace-domain analysis of uniformly-sampled pulse-width modulators," in *Proc. IEEE 35th Annu. Power Electron. Specialists Conf.*, pp. 4292–4298, vol. 6, 2004.

[38] R. Middlebrook, "Predicting modulator phase lag in PWM converter feedback loops," in *Proc. Powercon*, 1981, vol. 8, pp. 1–6.

[39] Y. Qiu, M. Xu, J. Sun, and F. C. Lee, "A generic high-frequency model for the nonlinearities in buck converters," *IEEE Trans. Power Electron.*, vol. 22, no. 5, pp. 1970–1977, Sep. 2007.

[40] X. Li, X. Ruan, Q. Jin, M. Sha, and C. K. Tse, "Small-signal models with extended frequency range for DC–DC converters with large modulation ripple amplitude," *IEEE Trans. Power Electron.*, vol. 33, no. 9, pp. 8151–8163, Sep. 2018.

[41] H. Tian, Y. W. Li, and Q. Zhao, "Multirate harmonic compensation control for low switching frequency converters: Scheme, modeling, and analysis," *IEEE Trans. Power Electron.*, vol. 35, no. 4, pp. 4143–4156, Apr. 2020.

[42] J. Lin *et al.*, "Accurate loop gain modeling of digitally controlled buck converters," *IEEE Trans. Ind. Electron.*, vol. 69, no. 1, pp. 725–739, Jan. 2022.

[43] D. Yang, X. Ruan, and H. Wu, "A real-time computation method with dual sampling mode to improve the current control performance of the LCL-type grid-connected inverter," *IEEE Trans. Ind. Electron.*, vol. 62, no. 7, pp. 4563–4572, Jul. 2015.

[44] L. Corradini, E. Orietti, P. Mattavelli, and S. Saggini, "Digital hysteretic voltage-mode control for DC–DC converters based on asynchronous sampling," *IEEE Trans. Power Electron.*, vol. 24, no. 1, pp. 201–211, Jan. 2009.

[45] G. Ripamonti *et al.*, "A dual-edge pulsewidth modulator for fast dynamic response DC–DC converters," *IEEE Trans. Power Electron.*, vol. 34, no. 1, pp. 28–32, Jan. 2019.

[46] H. Abedini and P. Mattavelli, "An oversampled hysteresis modulation for shaping the output impedance of droop-controlled boost converters in DC microgrids," in *Proc. IEEE 4th Int. Conf. DC Microgrids*, 2021, pp. 1–6.

[47] T. Sakharuk, B. Lehman, A. Stankovic, and G. Tadmor, "Effects of finite switching frequency and delay on PWM controlled systems," *IEEE Trans. Circuits Syst. I, Fundam. Theory Appl.*, vol. 47, no. 4, pp. 555–567, Apr. 2000.

[48] H. d. T. Mouton, S. M. Cox, B. McGrath, L. Risbo, and B. Putzeys, "Small-signal analysis of naturally-sampled single-edge PWM control loops," *IEEE Trans. Power Electron.*, vol. 33, no. 1, pp. 51–64, Jan. 2018.

[49] M. Berg and T. Roinila, "Nonlinear effect of dead time in small-signal modeling of power-electronic system under low-load conditions," *IEEE Trans. Emerg. Sel. Topics Power Electron.*, vol. 8, no. 4, pp. 3204–3213, Dec. 2020.

Ivan Z. Petric (Student Member, IEEE) was born in Belgrade, Serbia, in 1994. He received the B.S. and M.S. degrees in electrical engineering from the University of Belgrade, Belgrade, Serbia, in 2017 and 2018, respectively. He is currently working toward the Ph.D. degree with Power Electronics Group, Department of Information Engineering, University of Padova, Padova, Italy.

From 2018 to 2019, he was a Researcher with Power Electronics, Machines and Control Group, The University of Nottingham, Nottingham, U.K. His research interests include modeling and digital control of power converters, grid-connected converters for renewable energy sources and smart microgrids, and electrical drives.

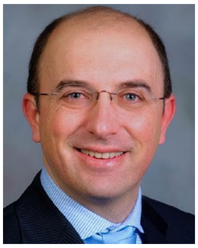

Paolo Mattavelli (Fellow, IEEE) received the M.S. (Hons.) degree and the Ph.D. degree in electrical engineering from the University of Padova, Padova, Italy, in 1992 and 1995, respectively.

From 1995 to 2001, he was a Researcher with the University of Padova. From 2001 to 2005, he was an Associate Professor with the University of Udine, where he led the Power Electronics Laboratory. In 2005, he joined the University of Padova, Vicenza, Italy, with the same duties. From 2010 to 2012, he was with the Center for Power Electronics Systems, Virginia Tech, Blacksburg, VA, USA. He is currently a Professor with the University of Padova. His research interests include analysis, modeling, and analog and digital control of power converters, grid-connected converters for renewable energy systems and microgrids, high-temperature and high-power density power electronics. In these research fields, he has been leading several industrial and government projects.

Dr. Mattavelli's current Google scholar H-index is 81. From 2003 to 2012, he served as an Associate Editor for the IEEE TRANSACTIONS ON POWER ELECTRONICS. From 2005 to 2010, he was the Industrial Power Converter Committee's Technical Review Chair for the IEEE TRANSACTIONS ON INDUSTRY APPLICATIONS. For terms 2003–2006, 2006–2009, and 2013–2015, he was a member-at-large of the IEEE Power Electronics Society's Administrative Committee. He was the recipient of the Prize Paper Award in the IEEE Transactions on Power Electronics in 2005, 2006, 2011, and 2012, and the 2nd Prize Paper Award at the IEEE Industry Application Annual Meeting in 2007. He is the Co-Editor-in-Chief for the IEEE TRANSACTIONS ON POWER ELECTRONICS.

Simone Buso (Member, IEEE) received the M.Sc. degree in electronic engineering and the Ph.D. degree in industrial electronics from the University of Padova, Padova, Italy, in 1992 and 1997, respectively.

He is currently an Associate Professor of electronics with the Department of Information Engineering, University of Padova. His main research interests include the industrial and power electronics fields and are related specifically to switching converter topologies, digital control of power converters, renewable energy sources, and smart microgrids.